A PHENOMENOLOGICAL INVESTIGATION OF IN-REACTOR CRACKING OF TYPE 304 STAINLESS STEEL CONTROL ROD CLADDING

M.P. MANAHAN, R. KOHLI

Battelle Columbus Division, Ohio, USA

J. SANTUCCI

Electric Power Research Institute, California, USA

and P. SIPUSH

Westinghouse Electric Corporation, Pennsylvania, USA

Wear and hairline cracking have been observed in the cladding of rod cluster control assemblies (RCCAs) in several pressurized water reactors (PWRs). The cracks are typically about 10 cm long, oriented longitudinally, and located in the high-fluence region of the rods. This paper reports our findings concerning the cause and nature of the cracking mechanism. Data from miniature-specimen tensile tests, scanning electron microscopy (SEM) investigations, and corrosion tests on control rod cladding that cracked in-service are reported along with the results of a hot cell investigation of an actual in-service crack. Possible causes of failure and comparisons to literature data are also presented.

1. Introduction

The Electric Power Research Institute (EPRI) initiated a study to develop new operating guidelines and inspection methods to help utilities predict and extend the service life of PWR control rods. The specific objectives of this program were to: correlate actual wear data on the RCCA rods with wear estimates from site photographs; determine the cause of cladding cracking; and estimate the performance of RCCAs while considering cladding wear and cracking. This paper reports primarily on our findings regarding the in-service cracking mechanism. Details of the overall test program are reported by Sipush et al. [1] and by Manahan and Kohli [2].

The mechanism of irradiation-assisted stress corrosion cracking (IASCC) has been suggested as a possible explanation for the observed RCCA failures. Recent constant extension rate tests by Clarke and Jacobs [3] on annealed Type 304 stainless steel (SS) revealed a fluence effect on intergranular stress corrosion cracking (IGSCC) resistance. Samples irradiated to a fast-neutron fluence ($E > 1.0$ MeV) of 3.0×10^{21} n/cm² were observed to fail entirely by IGSCC when tested in

561 K water containing 32 to 36 mg/l of dissolved oxygen. Another specimen irradiated to 1.0×10^{18} n/cm² was tested under identical conditions and failed in a ductile mode. Thus, there appears to be an incubation dose above which the microstructure evolves to a state that promotes IGSCC. This work demonstrates that the relative contribution of a corrosive medium on the fracture behavior is unknown since brittle fracture was observed to occur in an inert environment.

In the present study, miniature-specimen tensile tests, SEM investigations, and corrosion tests were performed on samples obtained from a PWR (Point Beach Unit 1) irradiated RCCA that experienced hairline cracking in service. The irradiated material was sectioned into four tube segments approximately 2.5 cm long. The tube segment identifications used are C (5.0×10^{21} n/cm²), D (4.0×10^{21} n/cm²), E (2.0×10^{21} n/cm²), and F (~ 0 fluence), in order of decreasing fluence.

2. Miniature-specimen tensile tests

Important constraints in selecting an appropriate test method were the limited amount of material availa-

Table 1

Miniature-specimen data for unirradiated Type 304 SS 10% cold worked tubing

Specimen no.	Miniature-specimen data [a]				
	Yield stress (MPa)	Ultimate tensile stress (MPa)	Uniform strain (%)	Fracture strain (%) (chart)	Fracture strain (%) (punchmarks)
1	558	753	32.8	46.8	48.5
2	593	767	28.2	43.1	47.1
3	589	769	32.2	44.3	53.9
Average	580	763	31.1	44.7	49.8
	Tube specimens – material lot certification data [a]				
				Fracture strain (%) (5 cm)	
1	589	754	not available	43.0	
2	587	748	not available	43.0	
3	589	762	not available	43.0	
Average	588	755	not available	43.0	
% difference of average properties	1.3	1.1	[b]	[b]	[b]

[a] All tests performed at room temperature in air.
[b] Data not available to allow meaningful comparison.

ble and the steep axial fluence gradient along the length of the control rod from which specimens could be obtained. Also, it was not desirable to perform tensile tests on the entire tube sections since this would severely limit the amount of data obtainable per unit volume. To satisfy these constraints, we used the patented Battelle miniature slow strain rate, tensile behavior test, developed by Manahan et al. [4]. Ten miniature tensile specimens can be obtained from a tube length of 23.0 mm which will yield data approximately equal in

accuracy to those for conventionally tested tube specimens.

To demonstrate the accuracy and validity of the miniature tensile specimens, three specimens were prepared from prototypic, unirradiated Type 304 SS tubing (10% cold worked [CW]) and then tested at room temperature and at a strain rate of 5.0×10^{-4} s^{-1}. The miniature-specimen results were compared with the results of uniaxial tensile tests on three tubes from the same lot of material. Test results are provided in table 1

Table 2

Postirradiation tensile properties of irradiated Type 304 SS 10% cold worked tubing determined using miniature specimens [a]

Specimen no.	Estimated fluence ($\times 10^{21}$ m/cm^2)	Strain rate (s^{-1})	IG/brittle fracture (%)	Yield stress (0.2% offset) (MPa)	Ultimate tensile stress (MPa)	Fracture stress (MPa)	Uniform strain (%)	Fracture strain (%)
C-1	5.0	5.0×10^{-4}	0	909	924	703	3.3	8.0
C-2	5.0	1.0×10^{-6}	3–4	936	944	708	1.6	9.3
C-3	5.0	2.0×10^{-7}	15–20	[b]	865	809	[b]	4.3
C-4	5.0	1.0×10^{-8}	30–35	[b]	848	577	2.6	6.8
D-1	4.0	1.0×10^{-6}	6	763	792	577	2.7	15.0

[a] The test temperature was 588 K and the atmosphere was argon gas for all tests reported here.
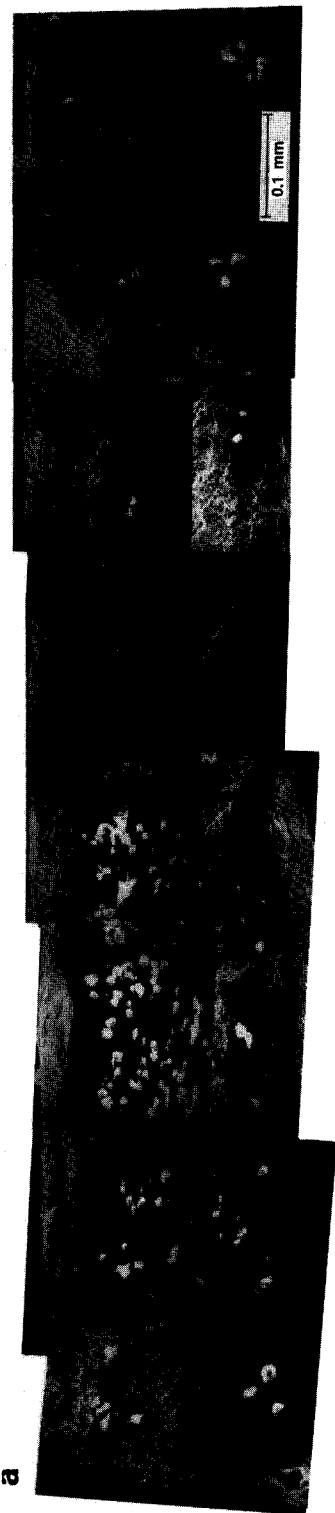[b] These data could not be reported due to uncertainty in the load-time record.

Fig. 1a. SEM micrograph of the fracture surface of specimen C-1. No evidence of IG cracking is observed.

which show that the miniature-specimen data were reproducible and compare well with the large specimen data. Comparing the average value of the yield stress (YS) and ultimate tensile stress (UTS) for the miniature and large specimens shows a 1.3% and 1.1% difference, respectively. We were unable to compare the uniform and fracture strains since sufficient large-specimen data were unavailable.

The main purpose of the postirradiation tensile tests was to determine whether the intergranular (IG) cracking mode observed in-reactor could occur in an inert atmosphere. Test results are given in table 2.

The first test (specimen C-1) was performed at a strain rate of 5.0×10^{-4} s^{-1} as a reference to compare with the unirradiated tensile properties of the material. A significant increase in the yield strength from 496 to 909 MPa (at 588 K) was measured. As expected, no IG fracture was observed due to the high strain rate. The next two tests (C-2 and D-1) were performed at a slow strain rate of 1.0×10^{-6} s^{-1}. In these tests, IG cracking was observed over a small percentage of the fracture surface. The effect of fluence and strain rate on the tensile behavior was evident. The next test (C-3) was run at a strain rate of 2.0×10^{-7} s^{-1}, which produced considerably more IG fracture; the fracture strain was also lower than in the previous tests. For specimen C-4, the strain rate was decreased to 1.0×10^{-8} s^{-1} and considerably more IG fracture was observed. The IG cracking always appeared on the inside surface (ID) of the specimen and initiated at about the same location. These data demonstrate that it is possible to obtain IG fracture in an inert environment above a threshold fluence. Also, the data further confirm that the amount
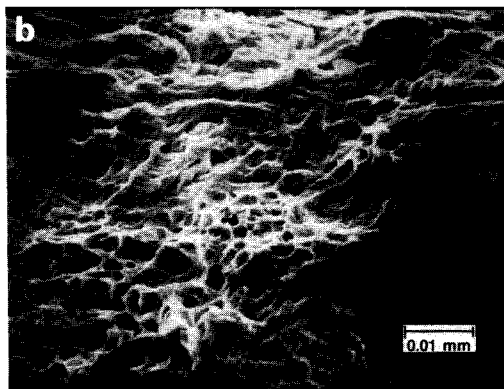

Fig. 1b. SEM micrograph of the fracture surface of specimen C-1 showing a typical ductile fracture surface.

of IG fracture is dependent on the strain rate for a given fluence.

During the tests for which there was IG fracture, we observed a rapid load drop. A correlation may exist between rapid load drop and IG cracking. A possible explanation is that a local critical stress σ^* is reached which is sufficient to initiate an IG crack. The load and load-carrying area of the specimen subsequently drop, and the crack arrests after propagating a short distance into a more ductile region. Cracking initiates again at the weakest spot in the gage section. Additional experiments are necessary to verify that this explanation is valid.

3. Microscopic examination and corrosion testing

3.1. Scanning electron microscopy

The fracture surfaces of the five tensile specimens, C-1, C-2, C-3, C-4, and D-1, were examined with an ISI Model Super II scanning electron microscope equipped with a Tracor Northern energy-dispersive (EDS) analyzer. Except for specimen C-1, which showed only the characteristic dimples typical of ductile fracture, the fracture surface of the other specimens revealed regions of brittle failure within a predominantly ductile fracture surface. Brittle fracture generally initiated intergranularly near one end of the specimen, although multiple regions of IG crack initiation were often observed on the ID of the specimens. Failure on the ID surface could be explained by the weakest link theory suggested above, by local stress variations due to bending from axial misalignment, or possibly by microstructural evolution. More experimentation is necessary to determine the precise cause.

The entire fracture surface of specimen C-1 is shown in fig. 1a. The surface shows the characteristic dimples, typical of ductile fracture (fig. 1b). No evidence of IG cracking was found.

Fig. 2a shows the fracture surface of specimen C-2. As in the case of specimen C-1, the fracture is predominantly ductile in nature, except for region 1-3, which shows IG fracture and where it appears the cracking initiated. This is clearly visible in the higher magnification micrographs shown in figs. 2b and 2c. Several particles (typical particles are marked 'A' and 'B' on fig. 2a) present in grain boundary locations in region 1-3 were analyzed by EDS. As shown in figs. 2d and 2e, some evidence for the presence of Si and S in the particles was obtained, suggesting possible radiation-enhanced impurity segregation in the alloy. The evi-
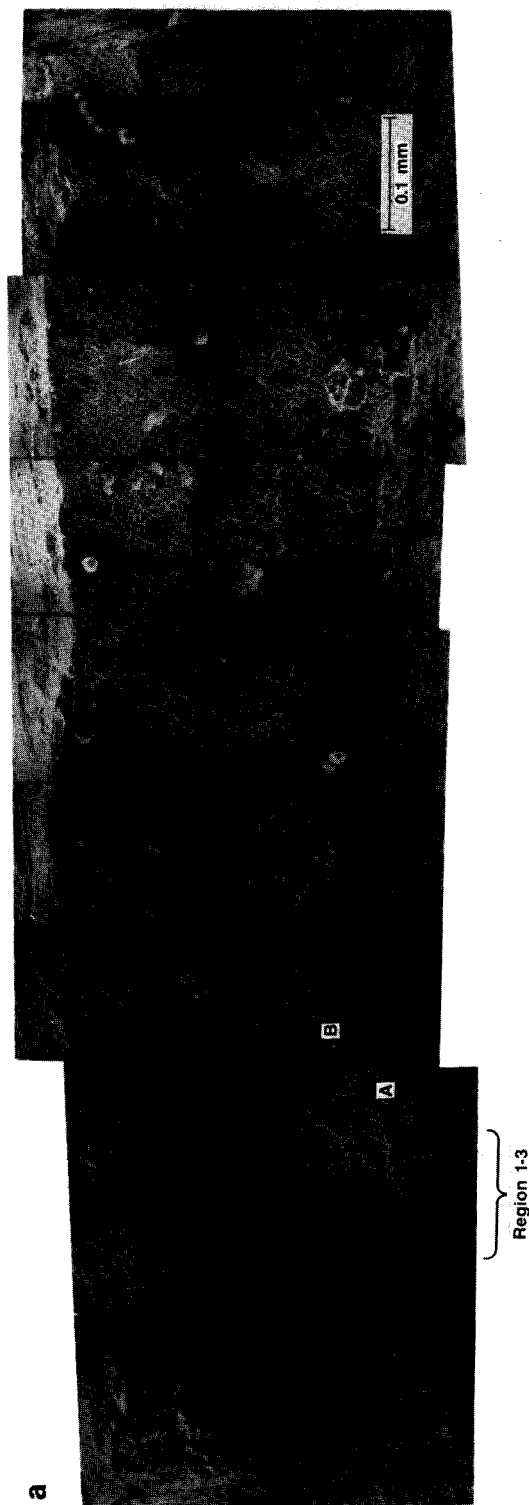

Fig. 2a. SEM micrograph of the fracture surface of specimen C-2. Region 1-3 shows IG fracture.
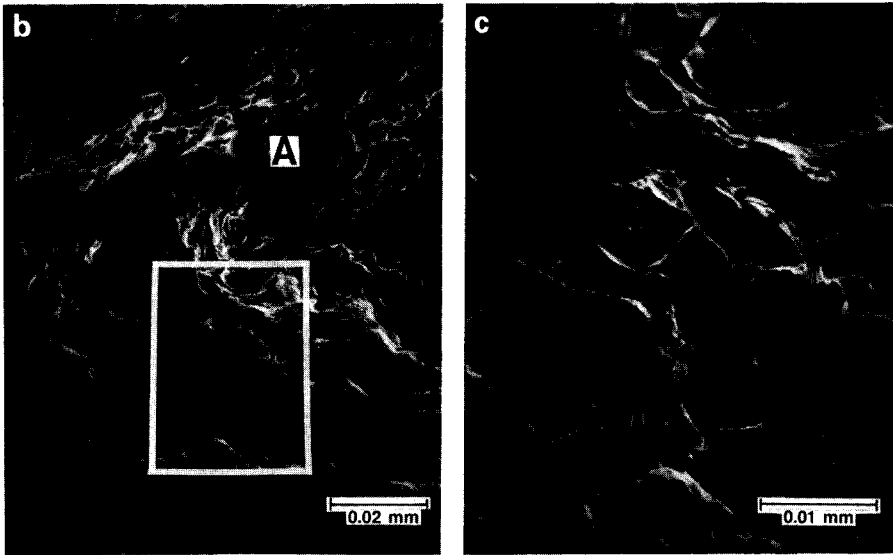
Fig. 2(b). SEM micrograph of region 1-3 of fracture surface of specimen C-2 at higher magnification showing IG fracture. Box enlarged in fig. 2c. (c). SEM micrograph of IG region 1-3 of fracture surface of specimen C-2 at higher magnification showing IG fracture. Box enlarged from fig. 2b.
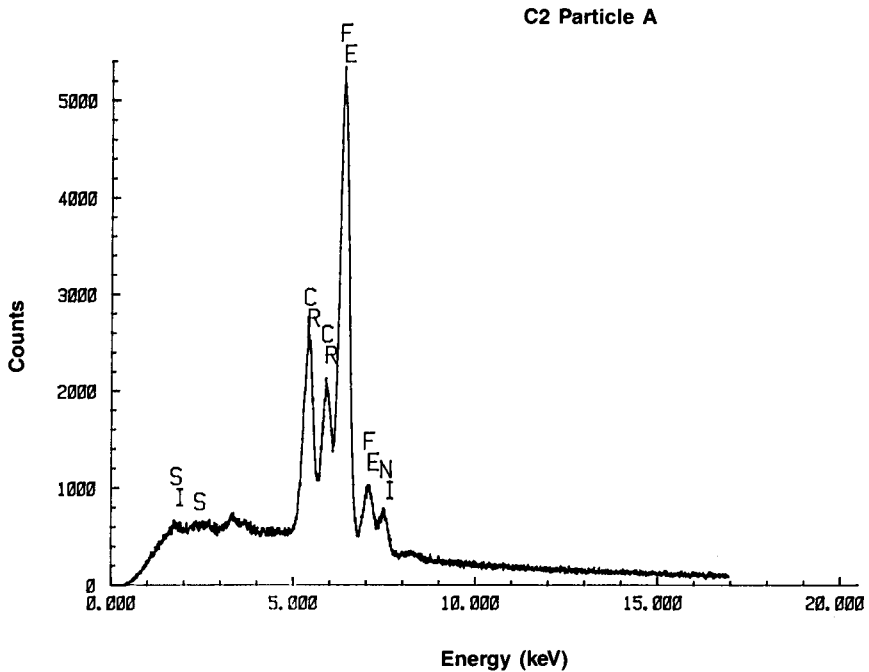

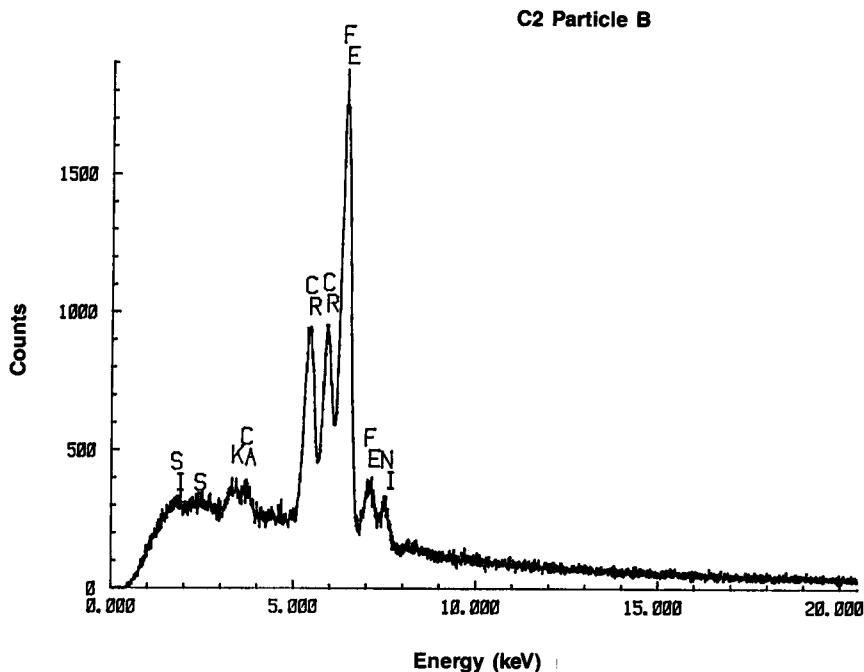Fig. 2d. EDS analysis of particle A found in specimen C-2.

C2 Particle B

Fig. 2e. EDS analysis of particle B found in specimen C-2.

dence for increased amounts of Si and S is limited since these peaks are only slightly above background. Based on the SEM observations, approximately 3 to 4% of the fracture is estimated to be IG in nature.

Specimen C-3 also showed a primarily ductile fracture surface, although about 15% is clearly IG in nature, as fig. 3a shows. The fracture appears to have initiated mainly intergranularly (region 1 in fig. 3a) near one end of the specimen, as shown in fig. 3b, although multiple regions of IG crack initiation can be seen on the ID of the specimen. Careful inspection of the entire surface did not reveal any particles and/or impurity segregation at the grain boundaries.

As shown in fig. 4a, for specimen C-4, the bulk of the fracture is ductile in nature, evidenced by the characteristic dimples typical of ductile failure. Approximately 30 to 35% of the fracture is brittle in nature, although clear evidence of IG rupture is lacking, suggesting that other failure modes, such as brittle shear, may also be operating (region 2-1 in fig. 4b). In common with the other specimens, the fracture appears to have initiated near one end of the specimen on the ID.

Careful SEM inspection of the entire fracture surface did not reveal any particles and/or impurity segregation at the grain boundaries.

The fracture surface of specimen D-1 reveals several interesting features. As shown in figs. 5a and 5b, approximately 5 to 6% of the fracture surface is IG in nature; otherwise the specimen ruptured in the ductile mode. Several particles were observed in the grain boundary regions (fig. 5a). EDS analysis (fig. 5c) revealed particle X to contain aluminum and nickel, suggesting the possible formation of a high-strength, low-ductility Ni_3Al intermetallic compound. Analysis of a second particle Y in the IG region showed the presence of zinc (fig. 5d), while a third particle Z contained sulfur (fig. 5e). According to Old [5], zinc is known to cause liquid metal embrittlement of austenitic stainless steels, while sulfur causes stress corrosion cracking (SCC).

It is not clear at present whether the particles seen can be attributed to radiation enhanced segregation or to inclusions in the steel. Additional data are necessary to establish a clear trend. It can be stated with certainty

Fig. 3a. SEM micrograph of the fracture surface of specimen C-3. Region 1 shows IG fracture.

that some microstructural change takes place which causes brittle fracture to occur at low strain rates after some minimum fluence.

3.2. Corrosion testing and metallographic examination

The nitric acid–dichromate corrosion test was used to determine the extent of IG penetration. This test is used extensively for determining the extent of IG attack in unirradiated stainless steels [1,6–8] by measuring weight loss and depth of penetration of the grain boundaries.

Corrosion coupons, approximately 0.3 cm long, were cut from the grip sections of the tensile samples C-2 and D-1, while corrosion coupons from the two other specimens E-3 and F-3 were cut from machined blanks. The coupons were deburred and then ultrasonically cleaned in alcohol and dried. Dimensions of the coupons were measured with a calibrated micrometer to determine surface area and the coupons were weighed before corrosion testing.

The C-2 coupon was submerged in a boiling solution of 5N HNO_3 containing 11.317 gm of $K_2Cr_2O_7$ per liter. It was weighed at 4 h exposure intervals until either a weight loss of 40 mg/cm^2 was obtained, or the specimen had been exposed for a total of 12 h, at which time the total weight loss was recorded. Previous work had shown these criteria to adequately corrode the specimens to determine the extent of IG penetration. Once the test duration (12 h) had been established with specimen C-2 by one of these two criteria, the remaining three specimens were individually tested according to the established criterion of 12 h of exposure.
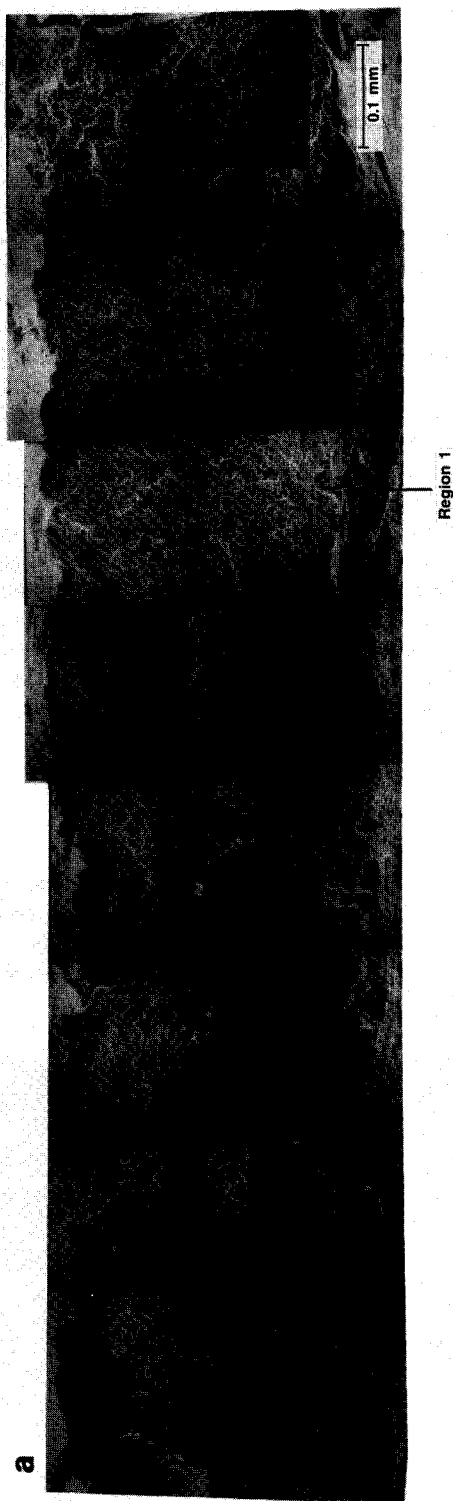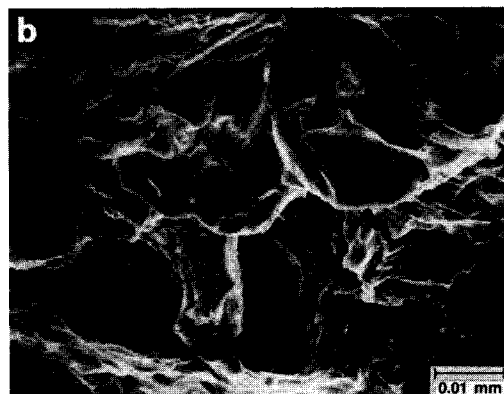

Fig. 3b. SEM micrograph of the IG region 1 of the fracture surface of specimen C-3 at higher magnification.

Fig. 4a. Fracture surface of specimen C-4.

At the end of the corrosion tests, each specimen was examined metallographically and photographed at sufficiently high magnification to permit the measurement of the depth of IG penetration. The weight change data for each specimen following 4, 8, and 12 h exposure times are given in table 3. Specimens C-2, D-1, and E-3 were taken from the rodlet tip in order of decreasing fluence. Specimen F-3 was taken from the upper end of the rod far from the tip where the fluence is several orders of magnitude lower, and hence was considered to be an unirradiated specimen. The results show a significant increase in the weight loss for the irradiated samples. This is consistent with the findings of Duncan [10] and others. Also, the irradiation effects appear to have saturated as no trend with fluence is discernible (specimens C-2, D-1, and E-3).

A slight trend in the average penetration depth of the grain boundaries with fluence was observed. For specimen C-2 with the highest fluence, clear grain boundary penetration was observed even with significant surface corrosion (see fig. 6). The grain boundary penetration was not distinct, however, for specimens D-1 and E-3, as the penetration was masked somewhat by general surface dissolution. For the low fluence sample (specimen F-3), clear grain boundary penetration was observed with little surface corrosion.

4. Control rod failure analysis

At Point Beach Unit 1, two cracked rodlets were found after 11 cycles of operation. Both cracked rodlets were in RCCA R26; one of these, rodlet 11, was destructively examined in the hot cell, along with refer-
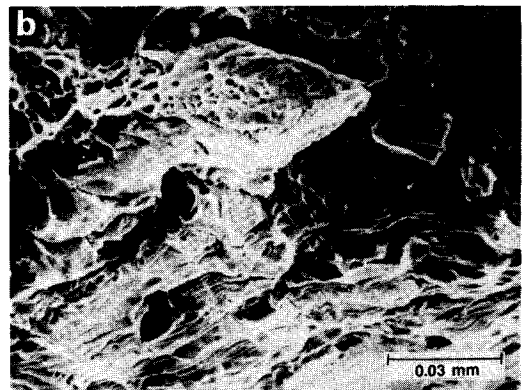

Fig. 4b. Region 2-1 of the fracture surface of specimen C-4 at higher magnification showing IG failure mode.

ence rod 16, which was not cracked. The observed cracks were located near the rodlet tips and were approximately 10 to 15 cm long.

Table 4 reveals the scope of the destructive examinations performed on the two rodlet tips showing the number of samples for each test and the measurements conducted. In addition, nondestructive visual (photography) and profilometric examinations were also performed. These measurements were performed on a cracked rod (rod 11) and an uncracked rod (rod 16), referred to as the reference rod/tip herein.

Fig. 7 shows the sectioning diagram for the reference tip (rod 16), indicating the locations of the various samples. Hardness measurements were performed on the metallographic samples near the rod tip and along the length of the rod. Micrometer and density measurements and a nitric acid-dichromate corrosion test were also performed near the tip of the rod. Fig. 8 shows the locations of the metallographic and the SEM samples for rod 11.

4.1. Metallography

4.1.1. Reference tip (rod 16)

Metallography samples were taken near the bottom and at 15 cm from the bottom of the absorber. Fig. 9 shows photographs of the radial gap between the absorber and the cladding at the two positions. These photographs were taken to determine the cladding/absorber gap and cladding thickness, and they show the circumferential location of the largest gap.

At the position near the bottom of the absorber (fig. 9a), it can be seen that the gap is much smaller than at the 15 cm position (fig. 9b). Also, rougher edges of the absorber outside diameter (OD) and cladding ID surfaces indicate that contact occurred at reactor temperature. When the cold-to-hot gap change is considered, contact would be expected at this position, whereas contact would not be predicted at the 15 cm position. There was no evidence of cladding wear in this sample, and the average cold diametral gap measured at this location was 1.3×10^{-3} cm. At the 15 cm position (fig. 9b) there is no evidence of absorber/cladding contact at temperature since the absorber OD and cladding ID surfaces are relatively smooth, and there is also no evidence of cladding wear. The average (cold) diametral gap measured at this location was 4.5×10^{-3} cm. The specified nominal as built gap was 7.6×10^{-3} cm.

The metallographic structure of the cladding is typical for Type 304 SS with 10% CW. Also, the seam weld was evident in all cladding metallography as a region of finer grain size. The reference tip metallography found

Fig. 5a. SEM micrograph of the fracture surface of specimen D-1. Region 3 shows IG fracture.
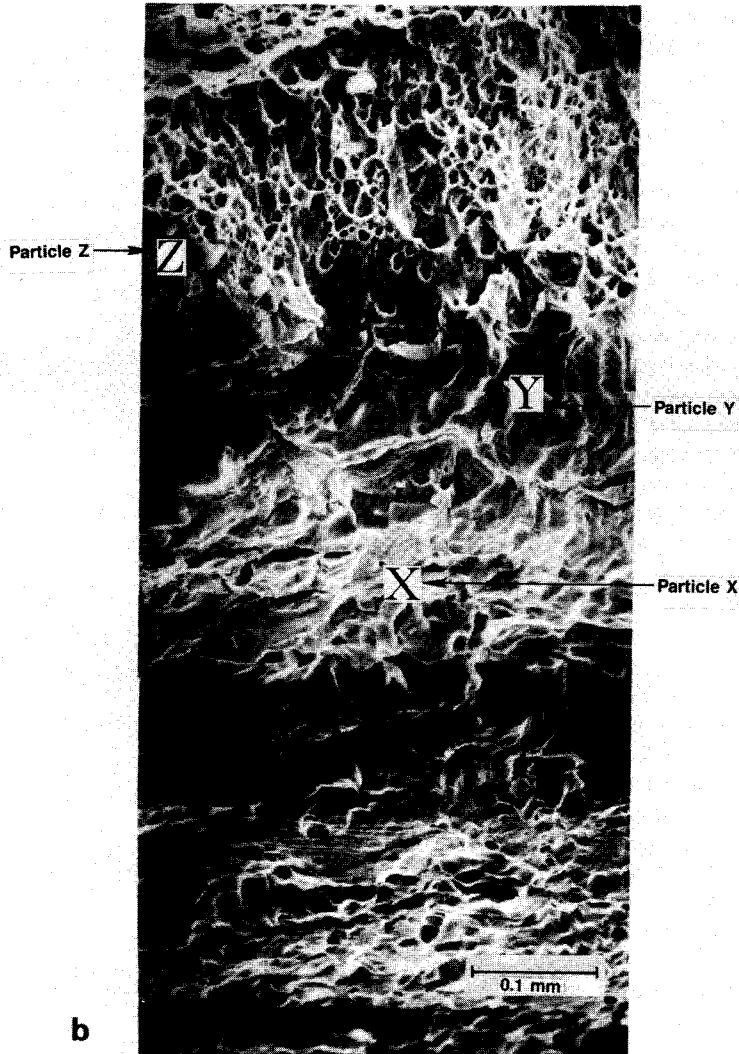
Fig. 5b. SEM micrograph of IG region 3 fracture surface of specimen D-1 at higher magnification.

near the bottom of the absorber a smaller diametral gap, evidence of absorber/cladding contact, no wear, and a normal seam weld. At 15 cm from the bottom of the absorber were found a relatively large diametral gap, no evidence of absorber/cladding contact, no wear, and a normal seam weld.

4.1.2. Cracked tip (rod 11)

Several metallographic samples were also taken in the region of the cracked tip. The first two were near the bottom of the absorber (sample L, same location as for the reference tip) and the other approximately 3.2 cm

from the bottom (sample M). After initial observations, additional samples were taken to further study the cracked tip (see fig. 8).

Fig. 10 shows some of the significant features of the 3.2 cm sample (sample M). Fig. 10a shows the full cross section of the penetrating crack. Local oxidation of the absorber can be seen opposite the crack, and the relatively smaller arc length of the absorber oxidation relative to the crack width suggests that the crack was opened further during rod cutting. Fig. 10b shows adherence of the absorber to the cladding near the crack, which is evidence of hard contact and perhaps chemical
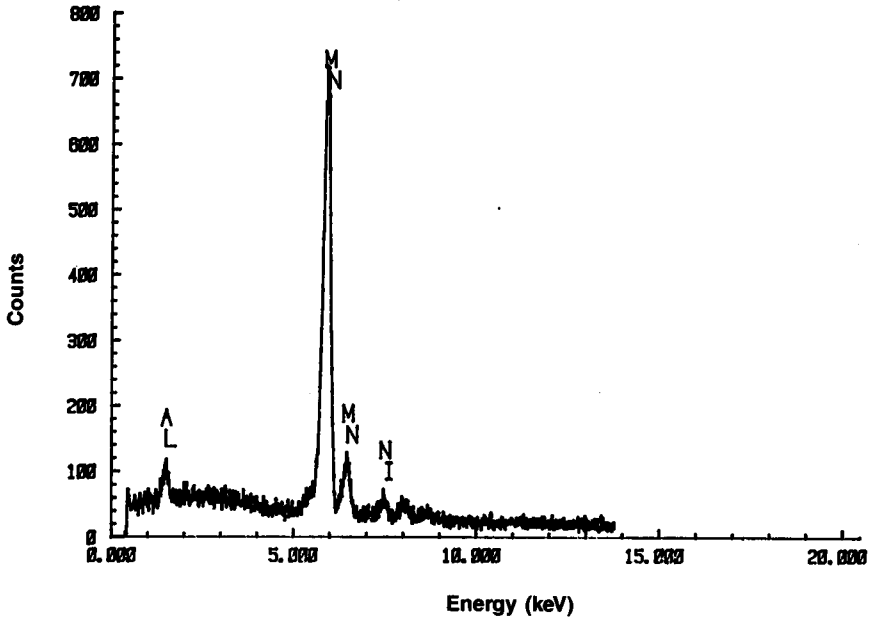
D1 Area #1 Part. X

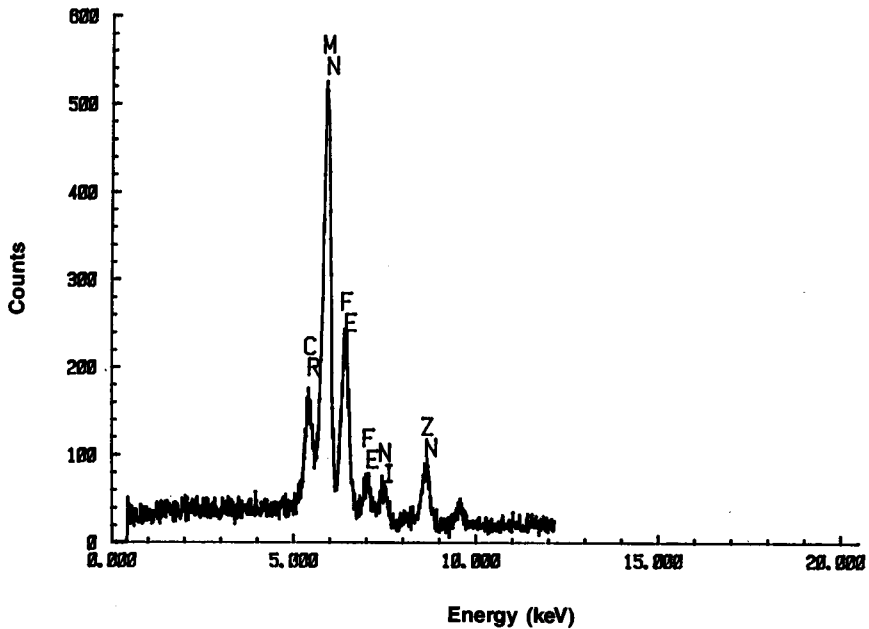Fig. 5c. EDS analysis of particle X found in specimen D-1.

D1 Area #1 Part. Y

Fig. 5d. EDS analysis of particle Y found in specimen D-1.
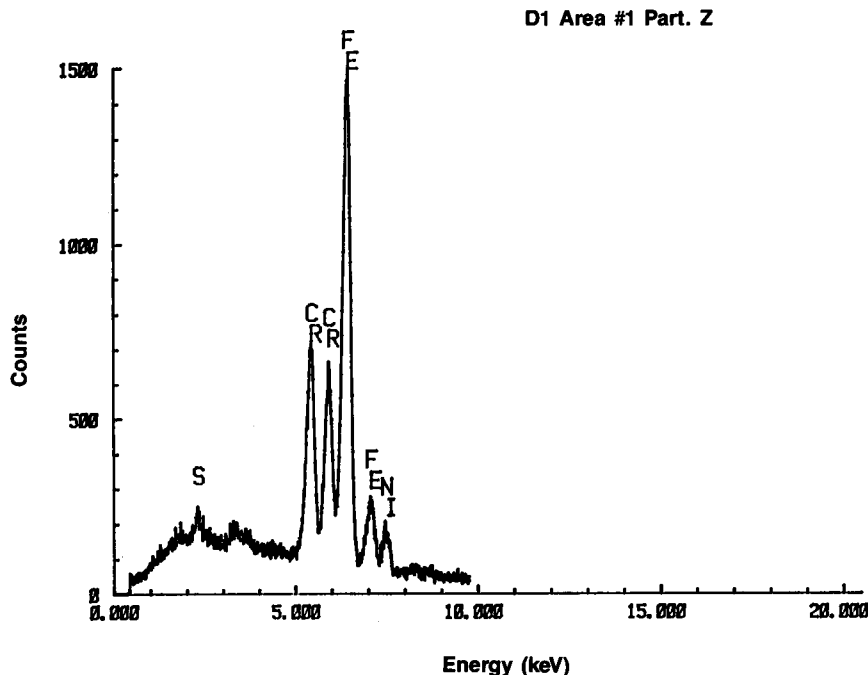
D1 Area #1 Part. Z

Fig. 5e. EDS analysis of particle Z found in specimen D-1.

interaction (diffusion) between the absorber and cladding. The cracking is IG in nature. Another significant finding is that the cladding wall was thinned approximately 5.0×10^{-3} cm near the crack, as determined from cladding thickness measurements. The measured average cold diametral gap (after correcting for crack width) is -6.6×10^{-4} cm, which indicates a small amount of absorber/cladding interference in the cold condition.

Fig. 11 shows optical micrographs of sample L from the cracked tip near the bottom of the absorber. Two

Table 3

Results of corrosion testing

Specimen no.	Weight loss (mg/cm^2) after			Estimated fluence ($\times 10^{21}$ n/cm^2)
	4 h	8 h	12 h	
C-2	4.43	21.30	60.75	5.0
D-1	+3.55 [a]	14.18	56.74	4.0
E-3	9.51	25.35	63.38	2.0
F-3	3.54	14.15	14.15	nil

[a] After 4 h Specimen D-1 exhibited a net weight gain of 3.55 mg/cm^2, which may be due to an atypical incubation period [9] in this specimen.

radial cracks, one of which is much narrower, are evident. Possible incipient cracks can also be seen at the OD of the cladding; however, it cannot be definitely concluded that the crack initiated at this location or from the OD, since the incipient cracks may have been due to a branching process from a higher elevation. No such incipient defects are seen at the 3.2 cm elevation. At the lower elevation, the IG nature of the crack is evident, and loose grains can be seen. Also, significant cladding wear of approximately 1.0×10^{-2} to 1.3×10^{-2} cm can be observed near the cracks by measuring the remaining cladding thickness. The measured average diametral gap (after correcting for crack width) is 1.1×10^{-3} cm, which is very similar to that for the reference tip.

Additional metallography was carried out on other samples from the cracked tip to determine the crack initiation location. These results are described below:

(a) Sample P. This sample was taken approximately halfway between samples L and M, about 1.52 cm from the bottom of the absorber. It appeared similar to sample M at the 3.2 cm position with a single crack; however, the width of oxidation near the crack tip was much larger. The measured diametral gap (after correcting for crack width) was -2.41×10^{-3} cm, which indicated considerable interference,

Fig. 6. Corrosion test metallography of specimen C-2.

Table 4

Scope of hot cell examination of control rod tips

| | Number of samples | |
	Cracked tip (Rod 11)	Reference tip (Rod 16)
Metallography	7 [a]	2
SEM	1	–
Absorber density	–	6
Chemical analysis (cladding)	1	–
Cladding hardness	–	4

[a] Sequential grinding on three samples.

even in the cold condition, and there was approximately 5.08×10^{-3} cm of cladding wear at the crack.

(b) Sample N. This sample was adjacent to sample L, near the bottom of the absorber, and facing up the rod. Metallographic examination results are shown in fig. 12. This figure shows that the second, smaller IG crack (seen in sample L, fig. 11) is now only part way through the cladding on the outside. This sample is only about 0.13 cm from sample L. The measured gap (corrected for crack width) from this sample is -1.35×10^{-3} cm, and the amount of cladding wear at the crack location is approximately 1.02×10^{-2} cm.

Fig. 13 shows the results of sequential grinding on sample N. After grinding away 0.12 cm, the second crack on the outside is even smaller and is joined with the primary crack (fig. 13a). A large secondary crack which joins the primary crack at both ends is also visible along with several smaller branching cracks. Fig. 13b shows the crack pattern after another 3.3×10^{-2} cm of grinding. The second crack no longer exists, but several branching cracks on either side of the primary crack can be seen.

(c) Sequential Grinding of sample L. In order to follow the two cracks observed in sample L in the other (downward toward the rodlet tip) direction, this sample was sequentially ground in 0.12 cm increments. The results showed that the second smaller crack no longer existed, but a small, possible incipient crack on the ID was seen near the primary crack.

(d) Sample O. This sample was located in the land area of the end plug. Further grinding of this sample verified that the crack ended above the circumferential end plug weld. Metallographic examination of a longitudinal sample of the plug end weld in the
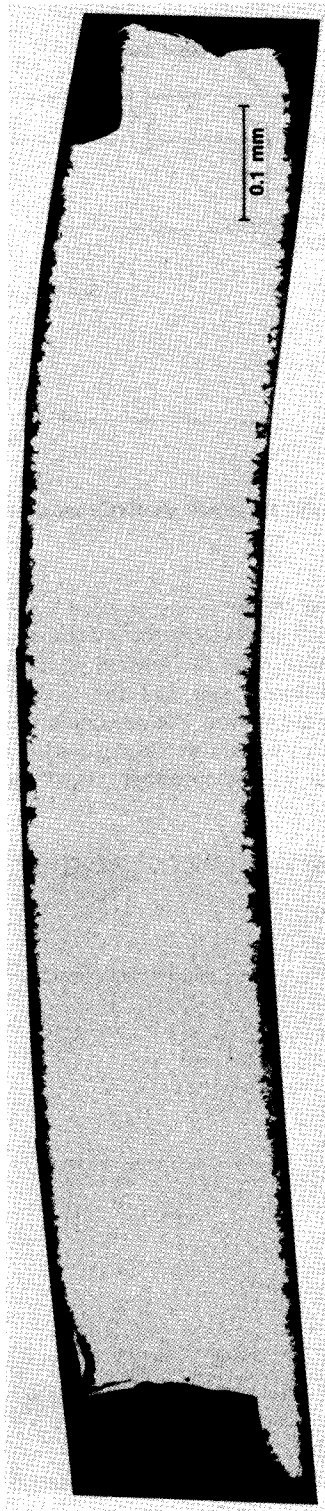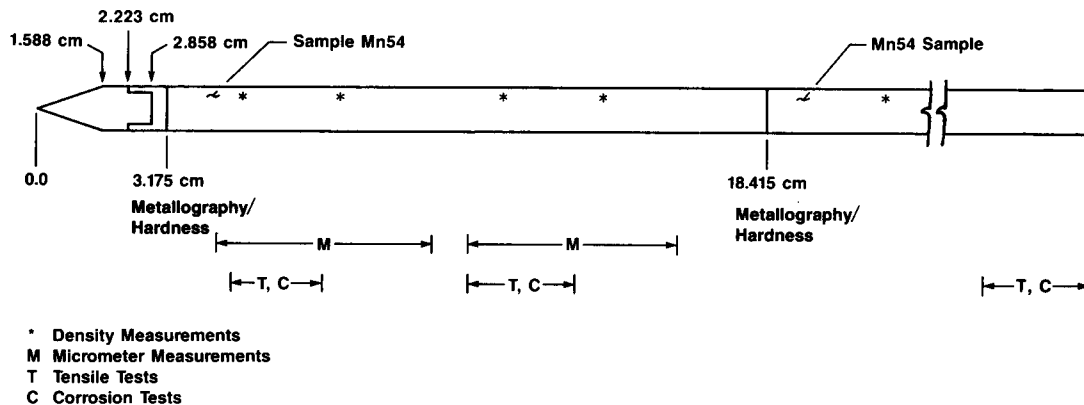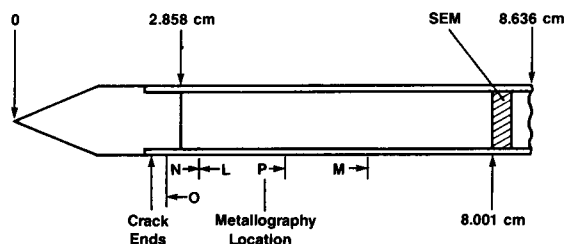
Fig. 7. Sectioning diagram for reference rod 16.

Fig. 8. Sectioning diagram for cracked rod 11. Sequential grinding performed at locations L, N, and O.

worn area below the crack showed that the weld was intact.

4.1.3. Discussion of results

Fig. 14 is a plot of the absorber/cladding gap as a function of distance from the bottom of the absorber. Both the 'as-measured' gap and the 'corrected' (for crack width) gap are shown. The maximum interference (-2.41×10^{-3} cm) occurs at approximately 1.52 cm from the bottom of the absorber. This interference
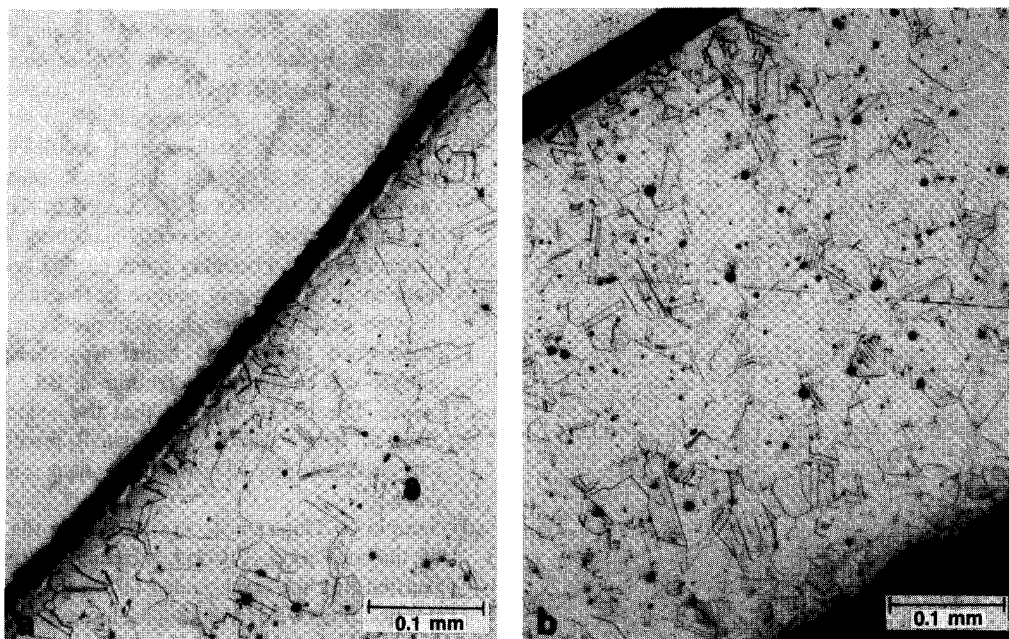

Fig. 9. Optical micrographs for reference tip 16: a. widest gap, bottom of absorber, b. widest gap, 15.24 cm from bottom of absorber.
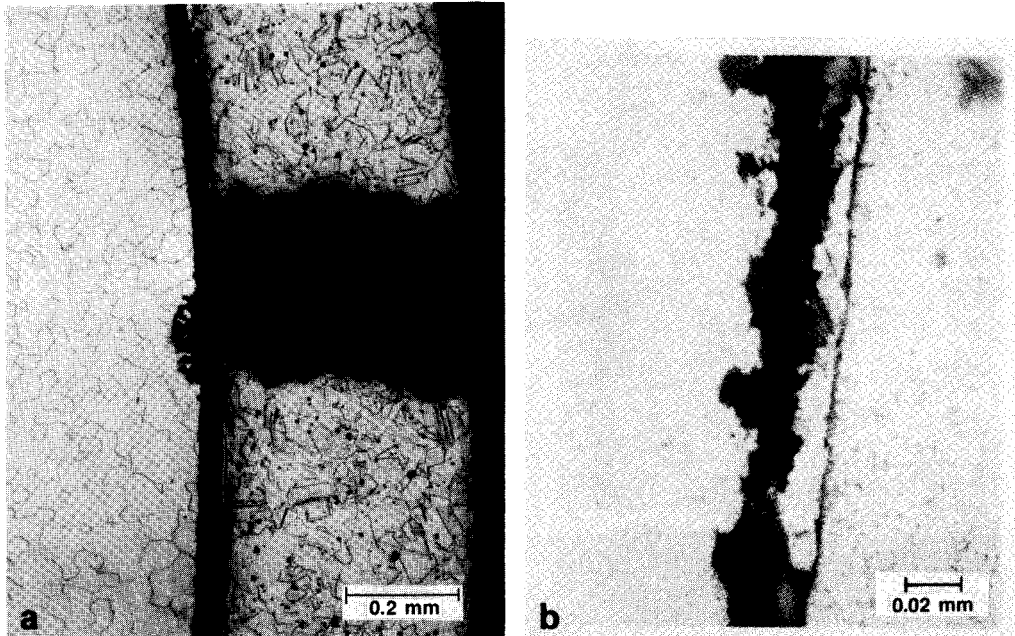
Fig. 10(a). Optical micrograph of sample M from the cracked tip at 3.2 cm from bottom of absorber. (b). Optical micrograph of sample M from the cracked tip at 3.2 cm from bottom of absorber.

would increase approximately 1.78×10^{-3} cm (to approximately -4.19×10^{-3} cm) at temperature in-service because of differential thermal expansion of the absorber and cladding materials. The interference at the time of actual cracking, however, is not known. The 1.52 cm location is also that of the maximum crack width in-pile, as determined from the oxide width in the absorber near the crack. Therefore, it is possible that the crack started at this location; however, it is uncertain whether the crack started on the cladding ID or OD.

The wear observed at the very bottom of the rod results from interaction with the fuel assembly thimble tube. This wear, observed in rod 11, most likely contributed to the cladding cracking as local wall thinning would cause an increase in any applied hoop stress. No wear was observed at the tip of the reference rod.

The cracked tip metallography indicates negative gaps (corrected for crack width), evidence of absorber/cladding contact, oxidation of absorber (enhanced near the crack), IG cracking, cladding wear in cracked area (crack occurred near maximum wear), and cracking away from the seam weld.

4.2. SEM results

The fracture morphology of the cracked rod is shown in fig. 15. The cracked cladding exhibited no ductility.

The crack is clearly IG in nature, and loose grains are evident. Elemental analysis of the inside and outside surfaces of the cladding showed the presence of silver on the inside surface, which is an indication of absorber/cladding contact. An elemental analysis of the inside and outside surfaces is given in table 5. It is instructive to compare these data with the chemical analysis of particles found in the fracture surface of the miniature tensile specimens machined from reference rod 16. These data are summarized in table 6. The ID surface of the cracked rod contained Al and Mn and these elements were also found in the miniature tensile specimens. The presence of Ag on the ID surface of the cracked rod may be due to diffusion after contact with the absorber.

4.3. Absorber / cladding gap and cladding strain

Profilometry diameter measurements using a knife-edge stylus (to eliminate off-center effects) are shown in fig. 16. The cracked tip diameters were corrected for the crack width from lead imprint measurements. There is no evidence of cladding permanent strain near the tip, the diameter is within the as-built tolerance range, and ovality, also evaluated at several locations near the tip, is less than 1.27×10^{-3} cm.

Fig. 17 shows the measured cold absorber/cladding diametral gap as determined from metallographic
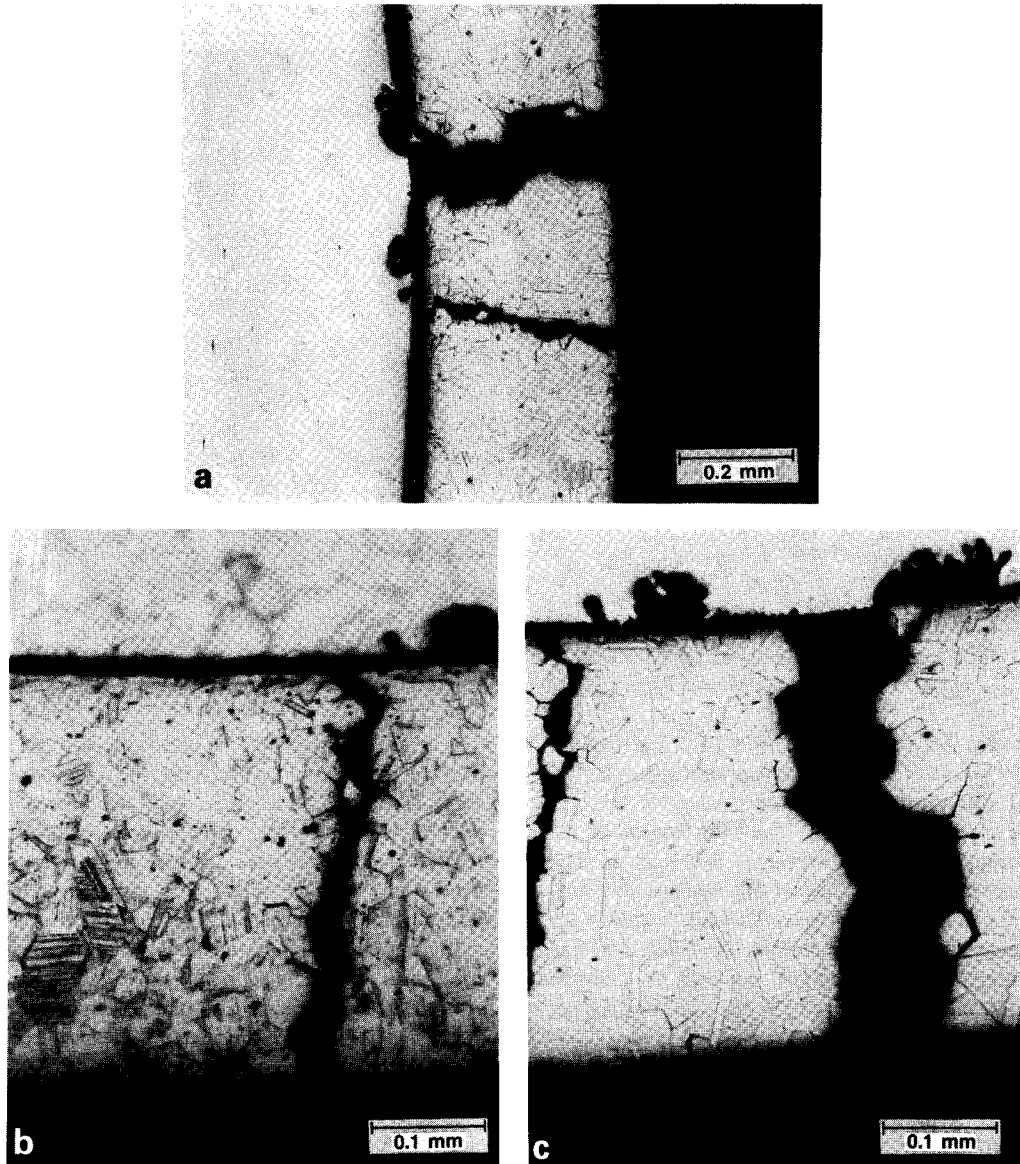
Fig. 11. Optical micrographs for sample L in the cracked tip near the bottom of the absorber: a. shows two radial cracks, b. shows possible incipient cracks on the OD, c. shows the two radial cracks at higher magnification.

examination along the entire length of rods 11 and 16. Included are the gaps measured at the tips (fig. 14). As can be seen, these gaps are greatly reduced in the tip region. (Gap sizes in the cracked tip were corrected for the crack width, as discussed previously.) Figs. 14 and 17 also show the estimated cold-to-hot gap change due to the higher thermal expansion of the absorber relative

to the cladding. Any gap smaller than this will likely produce interference between the absorber and cladding under hot conditions, resulting in tensile hoop stresses in the cladding. Hard contact would be expected at the bottom of the absorber, which agrees with the indications of contact in the metallography samples. The gaps in the top portion of the rodlets are the same for both
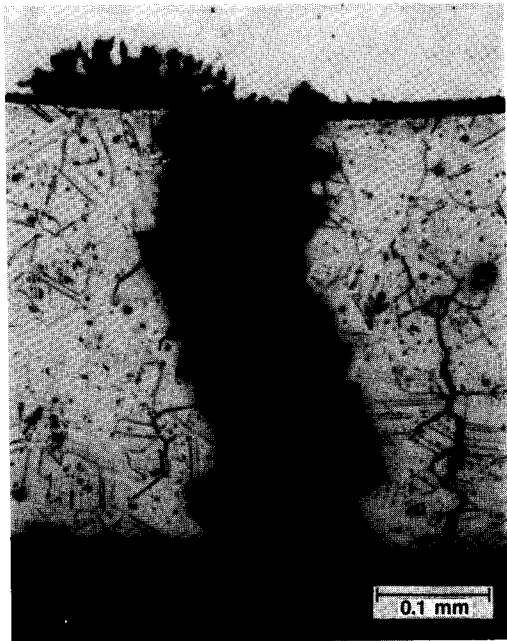
Fig. 12. Optical micrograph of sample N in the cracked tip near the bottom of the absorber.

Table 5

Semi-quantitative elemental analysis of cracked rod 11

Element	Inside surface (ID) (wt%)	Outside surface (OD) (wt%)
Si	1.1	1.8
S		1.0
Cr	12.7	23.5
Fe	36.9	56.6
Ni	5.2	13.9
Sn		2.4
W		0.8
Al	1.1	
Cl	0.2	
Mn	3.7	
Ag	39.1	

the cracked and reference rodlets, indicating that absorber oxidation after cracking did not lead to any significant dimensional changes in the cracked rodlet.

4.4. Absorber density measurements

The data above strongly suggest an absorber/ cladding mechanical interaction mechanism that would produce tensile stress in the cladding and that could
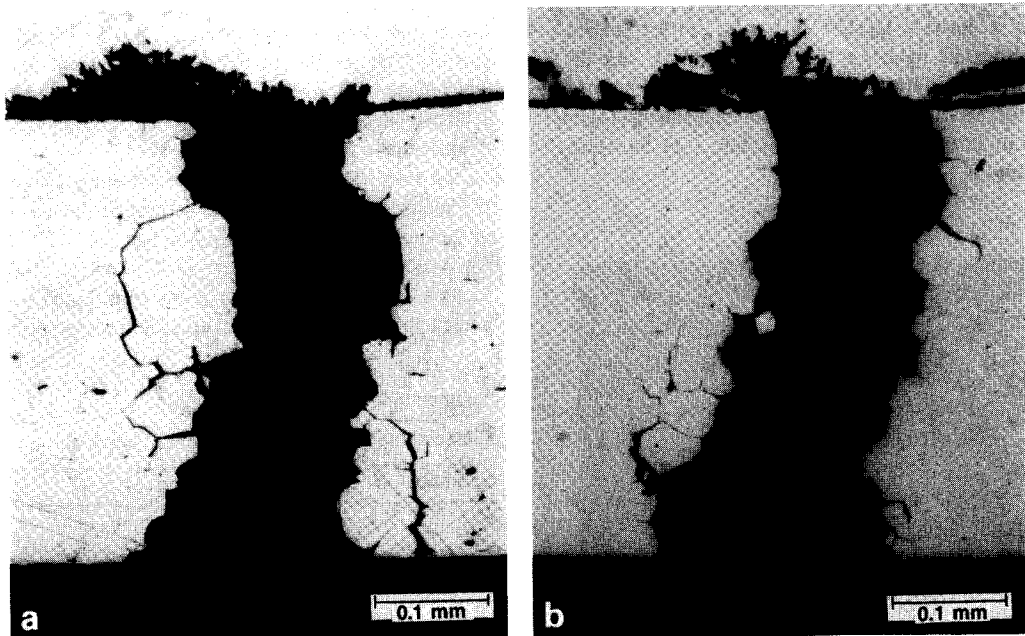

Fig. 13. Optical micrographs showing sequential grinding on sample N in the cracked tip near the bottom of the absorber: a. shows the crack pattern after 0.12 cm of grinding, b. shows the crack pattern after 3.3×10^{-2} cm of grinding.
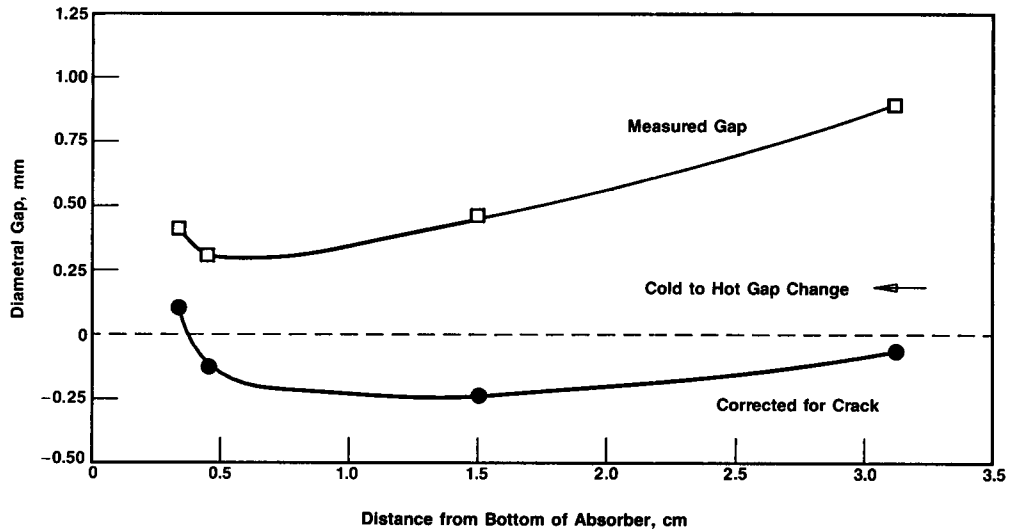
Fig. 14. Absorber/cladding gap for cracked rod 11.

cause cracking. The Ag-In-Cd absorber material is also known to swell under irradiation [6].

Before density measurements were performed, several of the key dimensions of the the absorber/cladding system were verified by means of detailed micrometer measurements on two sections of the reference rodlet at locations shown in fig. 7. Measurements of the cladding OD at two azimuthal locations, the cladding thickness at four azimuthal locations corresponding to the OD measurements, and the absorber OD at two azimuthal locations corresponding to the OD measurements were performed at intervals of approximately 1.27 cm along these segments.
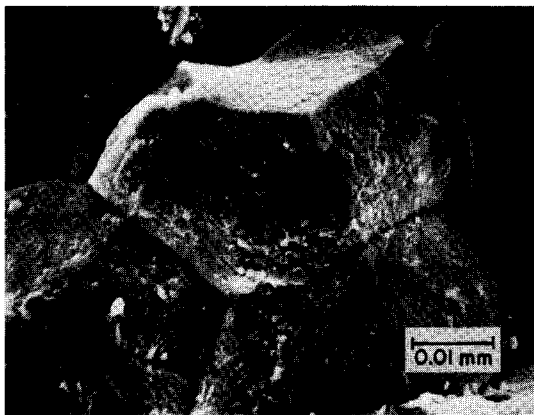
The results of these measurements are plotted in fig. 18. The absorber/cladding gap was calculated from the measurements and compared with previous metallography results; these results are also shown in that figure. The micrometer measurements agree well with the metallographic results at the 15.2 cm position and indicate that the gap did close near the bottom of the rodlet. From the absorber OD measurements, one can see that the Ag-In-Cd increased in size near the tip. This dimensional change corresponds to approximately 1.5% swelling relative to nominal dimensions, as indicated on the figure.

To confirm the amount of swelling, the density of the absorber material in the reference tip was measured at several locations, as indicated in fig. 7. The samples were made by cutting the two micrometer measurement samples and using pieces from other locations in the rodlet, including material several meters from the tip.

Fig. 15. SEM fracture surface of cracked rod 11.

Table 6

Elemental analysis of fracture surface particles

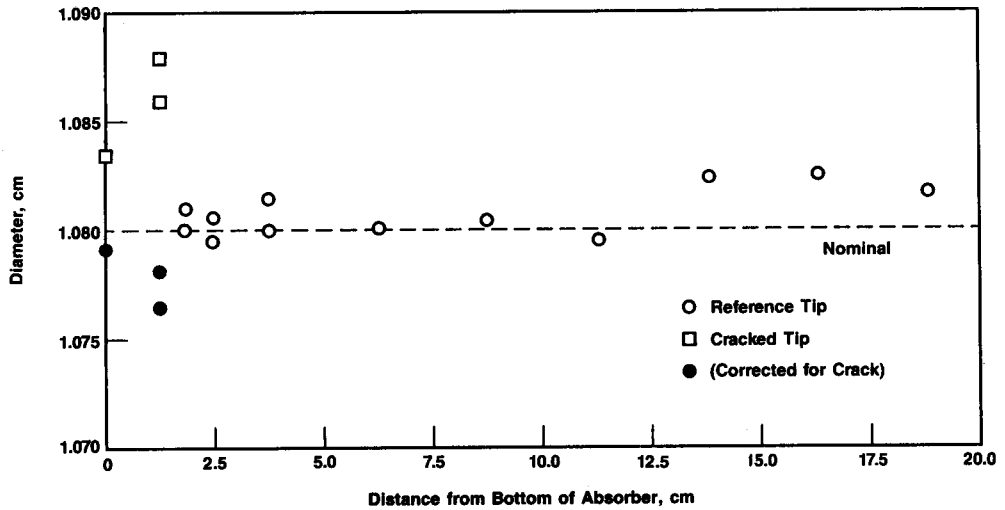| Specimen	Element
C-2	Si
	S
D-1	Ni
	Al
	Zn
	S
	Mn

Fig. 16. Knife edge profilometry diameter measurements for rods 11 and 16.

Density was determined from water displacement by weighing the samples in and out of water.

The density data are plotted in fig. 19. The density measured at the top of the rod agrees well with the unirradiated density of 10.17 g/cc [7]. The swelling near the bottom (0.75% density change) corresponds to an estimated fast fluence ($E > 1.0$ MeV) of approximately 5×10^{21} n/cm^2, resulting in a swelling rate of 0.15%
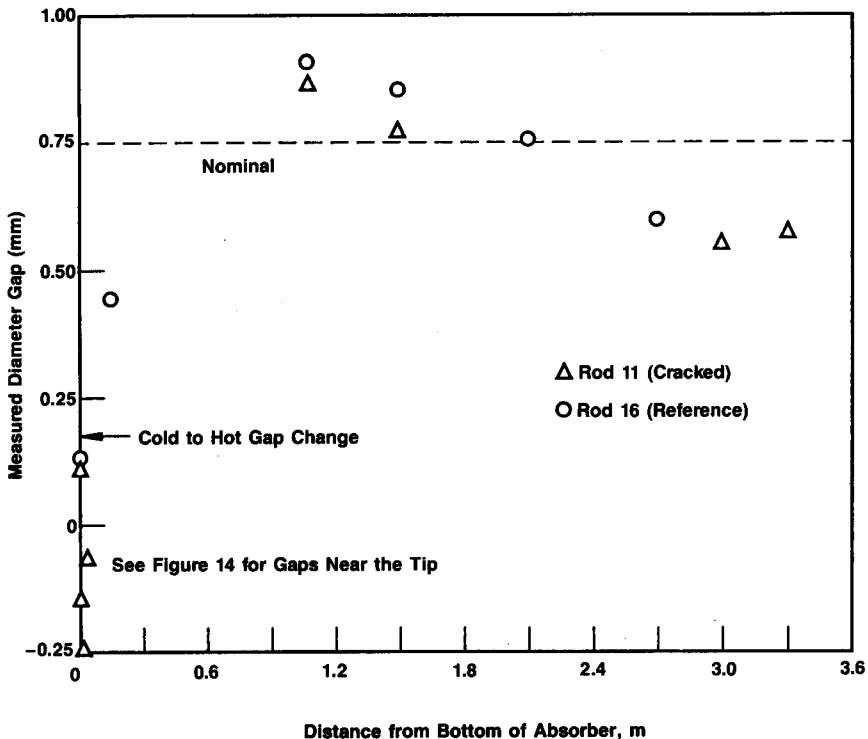

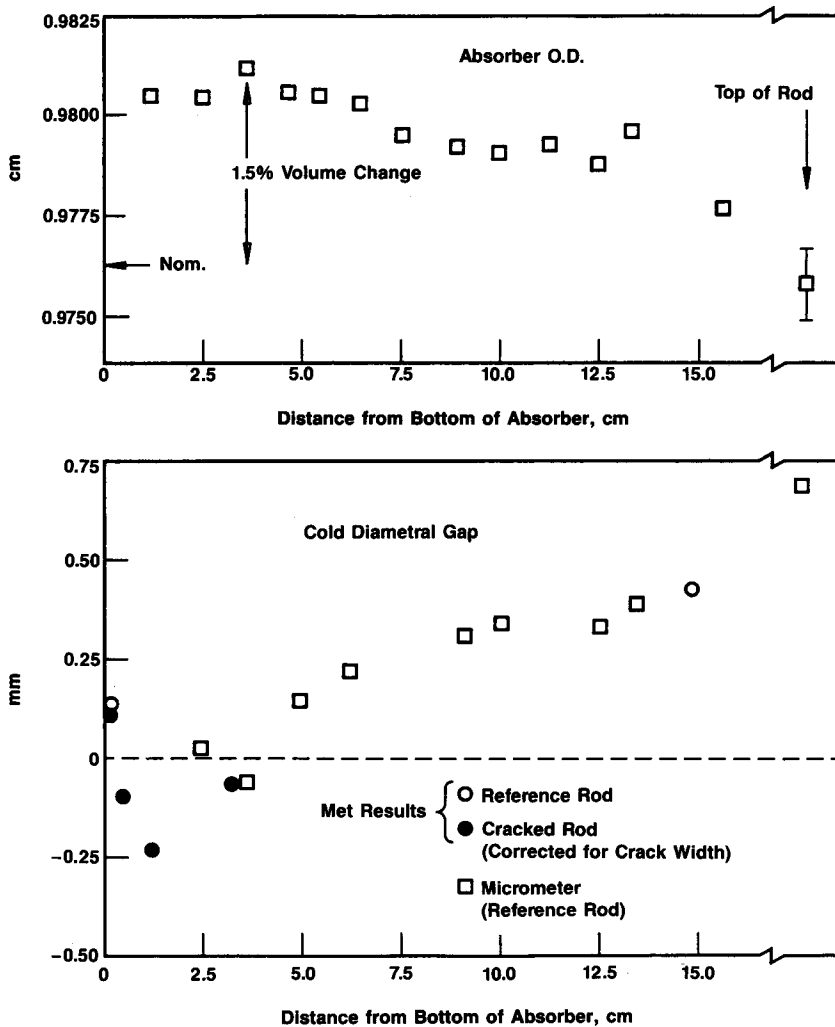Fig. 17. Measured diametral gap for rods 11 and 16.

Fig. 18. Absorber OD for rod 16 and cold diametral gap as a function of distance from the rodlet tip for rods 11 and 16.

per 10^{21} n/cm^2, which agrees reasonably well with the value reported previously [8]. The swelling in the reference rod at approximately 3.18 cm from the bottom of the absorber (1.5% volume change) is about half that determined from the micrometer measurements (fig. 18). This suggests that partial gap closure may have been due to some other mechanism such as plastic deformation (yielding) of the absorber due to axial forces during operation. The axial variation in the diametral gap shown in fig. 17 indicates that some axial redistribution of the absorber material may have occurred in service.

The above interpretation is based on nominal absorber dimensions. An alternative explanation would be to assume the as-built absorber diameter was at the upper tolerance limits. This would result in an inferred swelling that is more consistent with the density measurements and within the scatter of the density data. Because the as-built absorber diameter is not known, definitive conclusions cannot be made as to the effect of plastic deformation of the absorber.

5. Proposed fracture mechanism

Based on the fracture data on one cracked rod tip (rod 11) and one reference intact rod tip (rod 16), it appears that the cracking mechanism is related to
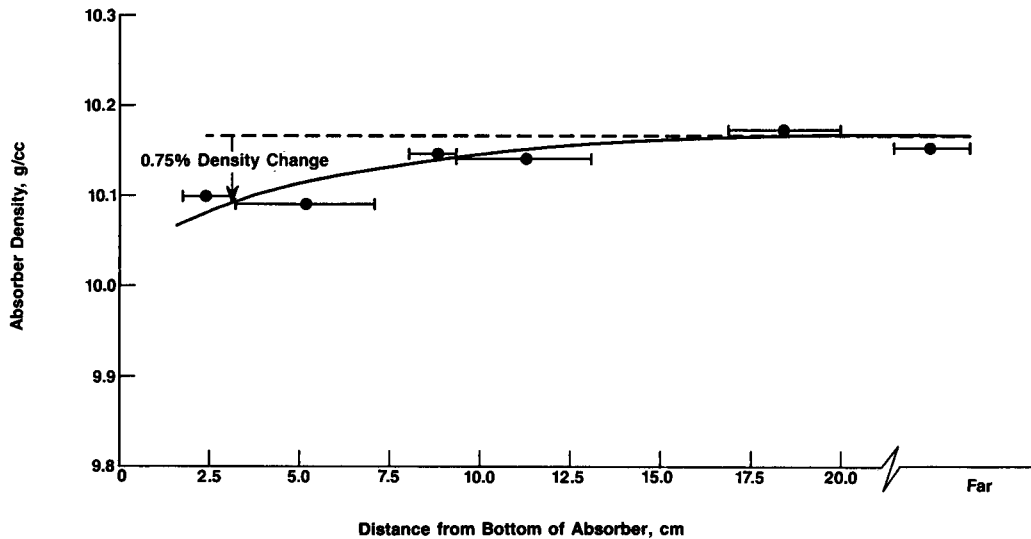
Fig. 19. Absorber density measurements for reference rod 16.

stresses produced by absorber/cladding mechanical interaction and to neutron damage of the cladding. The most probable effect of irradiation is radiation-enhanced segregation of the impurity elements to the grain boundaries, in agreement with Jones and Brimahll et al. [11,12]. Element diffusion between the absorber and cladding is also possible after contact. In-pile data from Garzarolli et al., indicate that cladding materials with reduced silicon and phosphorus are less prone to cracking [13].

Based on the results of the miniature tensile tests of irradiated cladding material in an inert environment, irradiation alone appears sufficient to render the cladding susceptible to IG cracking. The ID surfaces of the specimens tested were not exposed to coolant. Fig. 20 shows the percent IG fracture of irradiated cladding in an inert atmosphere as a function of strain rate. Autoclave tests representative of a typical PWR coolant would have to be performed at low strain rates to determine any contribution of the environment to the in-pile cracking. Such tests could determine the extent to which stress corrosion plays a role in the in-pile cracking mechanism.

The source of the stress that causes cracking in RCCA rodlets is absorber contact with the cladding. The magnitude depends on a combination of: absorber swelling, possible plastic deformation (yielding) of the absorber material due to axial forces during power stepping in-service, thermal expansion, tolerances, and wall thinning of the cladding due to wear caused by contact of the cladding with the fuel assembly guide
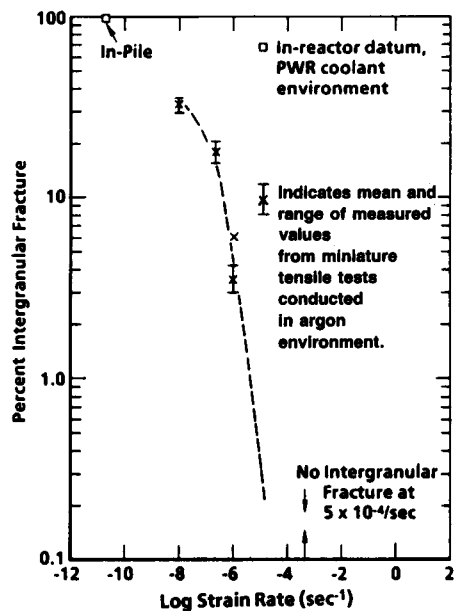

Fig. 20. Percentage IG fracture versus strain rate for irradiated cladding tensile tests at 588 K.

thimble at the rodlet tip. Absorber swelling, plastic deformation, and relative thermal expansion would contribute to absorber/cladding gap closure during service, and tolerances would affect the initial gap. Wall thinning would cause an increase in the local hoop stress in the thinned area. One of the most significant differences

between the cracked tip and the reference tip is the observed wall thinning in the cracked rodlet. The cracking occurred in the thinned area.

Metallographic examination of the cracked tip showed 100% IG fracture and no ductile fracture. The profilometry showed no plastic deformation of the cladding. These results, which indicate that the cracking occurred below the yield stress, are consistent with those of the tensile tests.

The cracking mechanisms appear to be generic; that is, cracking can occur in Type 304 SS cladding irradiated to high fluences, at stresses below the general yield stress, as a result of mechanical interaction between the absorber and the cladding. However, more data are needed to better quantity the influence of variables such as fluence, manufacturing tolerances, and number of axial power stepping events on the cracking frequency.

These cracks appear to have no impact on the performance of the Point Beach RCCAs up to 11 cycles of operation, since no evidence exists that longitudinal hairline cracks affect the functional requirements of an RCCA. However, the total functional lifetime of cracked RCCAs is at present undetermined. The rodlets do not become distorted as a result of the cracks, and no diameter increase was observed. Cracks are longitudinal and, although branching cracks are seen, they did not lead to separation of the component parts. The amount of absorber corrosion that occurred in the cracked rodlet due to coolant entering through the crack did not result in any degradation that affected RCCA functional requirements.

5.1. Comparison with literature data

The IASCC of Type 304 SS has been studied by several investigators [3,10,11,13,15–17]. Austenitic alloys exposed to high neutron fluences and radiolytic oxidizing radicals have failed intergranularly under
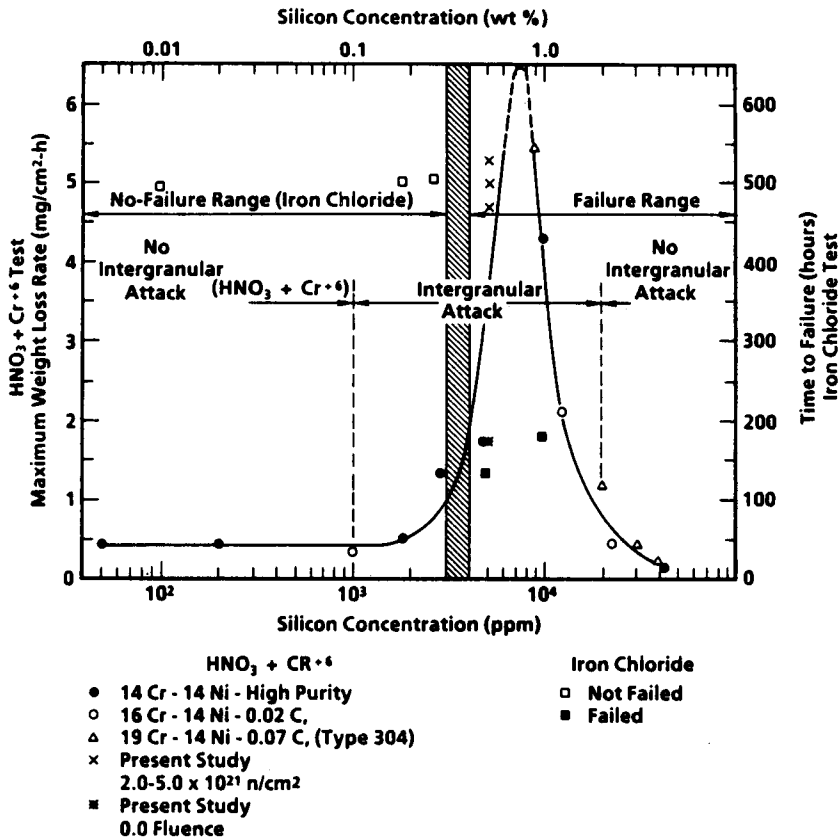

Fig. 21. Effect of silicon additions on the corrosion resistance of nonsensitized, high-purity SS alloys [10]. Data from present study are included.

tensile stress fields. In-reactor failure of Type 304 SS, 304L SS, 347 and 348 SS, Inconel 800 and 625, and other alloys has been observed for boiling water reactor (BWR) and PWR fuel rods, BWR control blade rodlets, sheaths and handles, neutron source holders, source range monitors, intermediate range monitors, and test capsules, according to Jacobs [14]. The cracking observed in the Point Beach PWR control rods may be another example of the same failure mechanism.

Armijo [15] and Aust [16] theorized that impurity segregation to the grain boundaries of austenitic alloys provides a continuous path for corrosion attack in the absence of a continuous carbide network in, for example, nonsensitized, solution-annealed material. In support of these theories, Duncan [10] found that carbon, silicon, and phosphorus at grain boundaries increased both IGSCC and IGSCC susceptibility of nonsensitized austenitic alloys.

Furthermore, irradiation was found to increase susceptibility of PWR and PWR SS fuel cladding samples irradiated to burnups of up to 35 MWd/kgU. In Duncan's work, the failure of cold worked and annealed irradiated SS fuel rod cladding was attributed to IASCC, where the applied tensile stresses resulted from pellet-

cladding mechanical interaction. High-purity SS was found to be more resistant to IGSCC both in the laboratory and during reactor service. Exposure to a boiling solution of nitric acid–potassium dichromate and exposure to a ferric chloride solution at 616 K provided consistent results that could be related to the in-reactor performance data. Figs. 21 and 22 compare literature data with those from this study. Test conditions for both sets of data were similar and the silicon and phosphorus concentrations for the present Point Beach specimens were taken to be the nominal values for this class of steel. The steel examined in this study contains silicon and phosphorus concentrations which would likely result in IG attack. IG failure, however, has been shown to occur in an inert environment. Additional work is needed to quantify the effects of a corrosive environment on the fracture behavior.

In another EPRI research program, Garzarolli and Stehle [17] tested several austenitic alloys under controlled strain rate conditions in both BWRs and PWRs. The results indicate a parabolic dependence of strain-to-failure on irradiation fluence. At fluences greater than about 6.0×10^{21} n/cm^2, materials that are susceptible to radiation-enhanced impurity segregation to grain
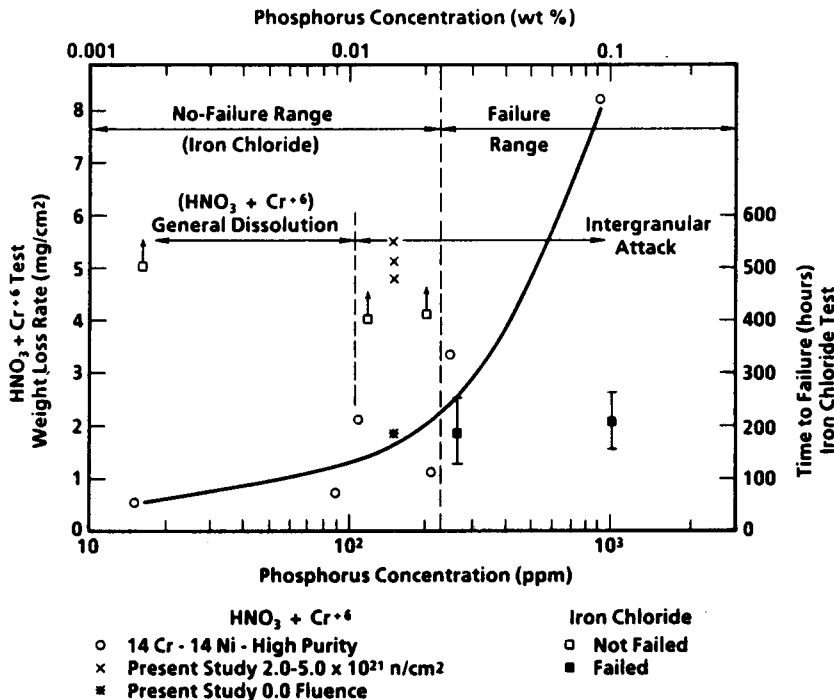

Fig. 22. Effect of phosphorus additions on the corrosion resistance of nonsensitized, high-purity SS alloys [10]. Data from present study are included.

boundaries, as well as to IG corrosion cracking, fail at essentially zero percent strain. These results are consistent with those observed on the Point Beach PWR components examined in the present study.

6. Summary and conclusions

The results of tensile testing and microscopic examination of irradiated RCCAs showed that a fast-neutron incubation fluence is necessary to change the material microstructure such that IG cracking is possible in irradiated Type 304 stainless steel (SS). IG fracture can occur in an inert environment in Type 304 SS provided that the material has been irradiated beyond the incubation fluence, and the strain rate is sufficiently low ($\leq 10^{-6}$ s^{-1}). IG failure may be more prevalent in irradiated 304 SS tested in a corrosive environment, but additional experimental work is necessary to confirm this.

Particles containing sulfur, silicon, aluminum, nickel, and zinc were observed in the grain boundaries of the highly irradiated Type 304 SS specimens, and radiation-enhanced diffusion could be responsible for this. The presence of these elements and the IG fracture region in the specimens suggest that more than one fracture mechanism could be operating in this material. Element and impurity transport could occur by clad/coolant interaction, clad/absorber interaction, and/or by radiation enhanced segregation to the grain boundaries.

Instances of IASCC in Type 304 SS and other austenitic alloys have been reported and analyzed for cases where the environment is highly oxidizing (BWRs). Cracking was found to occur in susceptible materials under conditions of very low stress. IASCC has also been observed in materials irradiated in less oxidizing environments (PWRs). At high exposures, susceptible materials have failed at relatively high applied loads. The data from Duncan [10] and from Garzarolli and Stehle [17] provide evidence for these phenomena, as do the results of investigations on the causes of fuel failure in 20 percent cold worked Type 304 SS clad fuel rods irradiated in a commercial PWR. The data from the Point Beach PWR components suggest that irradiation-assisted IG cracking of commercial-purity Type 304 SS can occur in PWR environments at very high exposures and under conditions of very low applied stresses. An important but as yet unresolved issue is the identification of the active corrodent in the PWR environment. In particular, it is not clear whether sufficient radiolytic oxidizing radicals exist in the PWR environment to

promote such failures, or whether other species in the coolant, such as LiOH, play an active role.

Acknowledgements

References

[1] P.J. Sipush, J. Woodcock and R.W. Chickering, Lifetime of PWR silver–indium–cadmium control rods, EPRI-NP-4512 (1986).

[2] M.P. Manahan and R. Kohli, in: Examination and testing of irradiated control rod tubing – Final report to Westinghouse Electric Corp, Battelle Columbus Division (1985).

[3] W.L. Clarke and A.J. Jacobs, Effect of radiation environment on SCC of austenitic materials, in: Proc. First Intl. Symp. on Environmental Degradation of Materials in Nuclear Power Systems – Water Reactors (August 22–25, 1983).

[4] M.P. Manahan, A.S. Argon and O.K. Harling, Determining mechanical behavior of solid materials using miniature specimens, US Patent Number 4,567,744 (1986).

[5] C.F. Old, Liquid metal embrittlement of nuclear materials, J. Nucl. Mater. 92 (1980) 2.

[6] K.D. Sheppard, S.R. Rajan and R.W. Chickering, Phase one interim report – Lifetime of PWR control materials, SMSC 84-172-1 (June 25, 1984).

[7] I. Cohen, The development and properties of silver-based alloys as control rod materials for pressurized water reactors, WAPD-214 (December, 1959).

[8] N. Fuhrman et al., Irradiation behavior of neutron absorber materials in Combustion Engineering's burnable poison and control elements, Topical Meeting on Light Water Reactor Fuel Performance, Orlando, Florida (April 21–24, 1985) pp. 5–13.

[9] A.J. Jacobs and G.E. Dunning, Correlation of weight and tensile strength loss with depth of intergranular attack in the HNO_3–Cr^{+6} corrosion test, Report No. A00-483, General Electric Company (1983).

[10] D.R. Duncan, Stainless steel failure investigation program final summary report; joint US-Euratom research and development program, EURAEC/GEAP-5530 (1968).

[11] R.H. Jones, Some radiation damage–stress corrosion synergisms in austenitic stainless steel, in: Proc. Second Intl. Symp. on Environmental Degradation of Materials in

Nuclear Power Systems – Water Reactors (September 9–12, 1985).

[12] J.L. Brimahll, D.R. Baer and R.H. Jones, Radiation-induced phosphorus segregation in austenitic and ferritic alloys, J. Nucl. Mater. 122&123 (1984) 196–200.

[13] F. Garzarolli, et al. Deformability of austenitic stainless and Ni-base alloys in the core of a boiling and pressurized water reactor, in: Proc. Second Intl. Symp. on Environmental Degradation of Materials in Nuclear Power Systems – Water Reactors (September 9–12, 1985).

[14] A.J. Jacobs, Effects of impurities and grain size on irradiation-assisted IGSCC of Type 304 SS and 348 SS, EPRI RP 2058-8 (1986).

[15] J.S. Armijo, Impurity absorption and intergranular corrosion of austenitic stainless steel in boiling HNO_3–$K_2Cr_2O_7$ solutions, Corr. Sci. 7 (1967) 143.

[16] K.T. Aust et al., Heat treatment and corrosion resistance of austenitic Type 304 stainless steel, Trans. ASM. 59 (1967) 544.

[17] E.F. Garzarolli and H. Stehle, Behavior of structural materials in LWR power reactors, in: Proc. Intl. Symp. on Improvements in Water Reactor Fuel Technology and Utilization, IAEA-SM-288/24 (September 15–19, 1986).